Solid State Phenomena
ISSN: 1662-9779, Vol. 390, pp 39-50
doi:10.4028/p-qK6j3v

Submitted: 2025-12-19
Revised: 2026-02-17
Accepted: 2026-02-24
Online: 2026-04-17

Laser-Induced Solid-State Foaming of HIPed Ti6Al4V-ELI Alloy

Guglielmi Pasquale[1,a*], Cusanno Angela[2,b], Piccininni Antonio[2,c], Fulco Emanuele[1,d], Sorgente Donato[2,e] and Palumbo Gianfranco[2,f]

[1]Department of Engineering, University of Basilicata, via Ateneo Lucano 10, 85100, Potenza, Italy

[2]DMMM - Politecnico di Bari, Viale Japigia 182, Bari 70126, Italy

[a*]pasquale.guglielmi@unibas.it, [b]angela.cusanno@poliba.it, [c]antonio.piccininni@poliba.it, [d]emanuele.fulco@unibas.it, [e]donato.sorgente@poliba.it, [f]gianfranco.palumbo@poliba.it

Keywords: Ti6Al4V-ELI alloy, laser-induced solid-state foaming, hot isostatic pressing, porosity evolution, material modelling.

Abstract. The present work proposes a novel strategy that significantly shortens Solid-State Foaming (SSF) times, delivering a substantial improvement in process efficiency and paving the way for faster production of customized and functionalized prosthetic components. In particular, the evolution of porosity was evaluated in terms of both volume fraction and mean pore diameter and its subsequent effect on microhardness in a Ti6Al4V-ELI alloy that was initially densified via Hot Isostatic Pressing (HIP) and then subjected to Laser-Induced Solid-State Foaming (LISSF). This acronym was introduced by the authors to underline the originality of this approach, which is not reported in the existing literature. Localized heat treatments were performed using a CO_2 laser source at a target temperature of 1020°C, with three distinct dwell times (120, 240, and 360 seconds). To predict density variations and the resulting mechanical properties, two analytical models were implemented and validated: (i) the Johnson–Mehl–Avrami–Kolmogorov (JMAK) kinetic model, which effectively described the time-dependent evolution of porosity and pore growth under different thermal regimes (based on conduction phenomena vs. direct laser exposure) and (ii) the Ryshkewitch-Duckworth (RD) model, which was used to correlate the exponential decay of microhardness with increasing porosity. The experimental results and regression analyses confirm the high predictive accuracy of both models (R^2 greater than 0.95), demonstrating the feasibility of the LISSF process for fabricating titanium components with locally controlled porosity for biomedical applications with reference to the manufacturing of customized and functionalized prosthetic components, ensuring both structural reliability and enhanced performance. On the other side, experimental results demonstrated that process parameters play a critical role in the microstructural evolution: specifically, increasing the dwell time to 360 s under direct laser exposure (1020°C) led to a maximum porosity fraction of approximately 30% and a growth in mean pore diameter up to about 35 μm.

Introduction

The growing demand for metallic materials with customized properties is fueling the development of innovative strategies for creating porous structures, particularly for biomedical and aerospace applications [1]. Among these, porous titanium alloys stand out for their unique combination of high specific strength and exceptional biocompatibility, making them the material of choice for orthopedic implants and lightweight structural components. In the biomedical field, controlled porosity promotes osseointegration and mitigates stiffness mismatch with bone, while in aerospace engineering, it enables significant weight reduction without sacrificing mechanical integrity [2].

Several techniques have traditionally been employed to introduce porosity into Titanium (Ti) alloys. Powder metallurgy and space-holder methods rely on removable agents during sintering, but often struggle to achieve uniform pore distribution and connectivity [3]. Additive manufacturing (AM) technologies, such as selective laser melting (SLM) and electron beam melting (EBM), have revolutionized the design of complex porous architectures with unparalleled precision; however, these processes remain energy-intensive and require advanced equipment [4]. Alternative approaches, including chemical foaming and gas-phase reactions, have also been explored, though they typically

involve intricate chemistries and may introduce contamination or compromise mechanical performance [5].

In this scenario, Solid-State Foaming (SSF) stands out as a key enabler for next-generation prosthetic manufacturing, combining structural reliability with tailored porosity for enhanced osseointegration [6]. In fact, by avoiding melting, SSF minimizes residual stresses, distortion, and microstructural degradation, ensuring the integrity of the original component. In particular, Laser-Induced Solid-State Foaming (LISSF) provides a means to introduce controlled porosity into Ti alloys while drastically reducing foaming time. Unlike AM, which constructs parts layer by layer, LISSF acts directly on fully dense components, locally inducing porosity through thermally activated mechanisms such as creep and diffusion, without melting the material. [7]. Moreover, its localized nature enables selective foaming in predefined regions, making it compatible with pre-existing parts and reducing processing costs compared to AM. A further advantage lies in its capability to create tailored porosity gradients within a single component, a feature particularly valuable for biomedical implants that require a dense core for load bearing and a porous surface to enhance osseointegration [8].

Supported by experimental findings, numerical modeling based on analytical formulations is essential for the design of manufacturing processes aimed at producing components with variable density through solid-state foaming. Such models enable the prediction of porosity evolution and resulting mechanical properties as functions of key process parameters, including temperature and dwell time [7]. This predictive capability allows engineers to optimize thermal cycles and foaming conditions to achieve tailored porosity gradients, which are critical for aerospace structures requiring weight reduction without compromising integrity. By minimizing trial-and-error and guiding process optimization, these models accelerate the development of tailored, high-performance components.

According to this, the present study investigates the application of LISSF to Ti-6Al-4V-ELI alloy previously densified by HIP. The research focuses on understanding porosity evolution – quantified by fraction (P) and average diameter (d) and its influence on mechanical properties (Vickers microhardness). To interpret and predict material behavior, two analytical models were employed: the Johnson–Mehl–Avrami–Kolmogorov (JMAK) model [9] with Arrhenius dependence, describing the kinetics of porosity growth and the Ryshkewitch–Duckworth (RD) model [10,11], correlating hardness with porosity. These models provide a physically meaningful framework for process optimization and pave the way for advanced applications where controlled porosity is critical.

Material and Methods

Material.

The proposed approach was focused on a Ti6Al4V-ELI produced by means of HIP. The chemical composition of the investigated material is presented in Table 1.

Table 1. Chemical composition (weight %) of the investigated Ti6Al4V-ELI.

Al%	V%	Fe%	C%	N%	H%	O%	Ti
6.21	3.80	0.16	0.008	0.011	0.001	0.008	Bal.

The material was produced through a HIP process carried out at 1000 °C under an applied pressure of 120 MPa, using titanium powders with an average particle size ranging from 70 to 100 μm and an argon content corresponding to a pressure of 0.4 MPa. According to this, the HIPed material is affected by the presence of reduced and pressurized microporosities (about 0.01 and 1 μm as P and d, respectively) [12].

Experimental Activity.

The LISSF experiments were carried out using a CO_2 laser source with a maximum power of 2.5 kW, combined with a LASCON® temperature control system which continuously controls the laser power to keep the temperature constant using data acquired by a pyrometer. As shown in

Fig. *1*a, the experimental setup features a square laser spot with a side length of 10 mm, kept fixed at the center of the specimen.

The sample is supported only at its ends, leaving the remaining part suspended and free from direct supports. This configuration ensures localized heating while minimizing mechanical and thermal stresses during each experimental test.

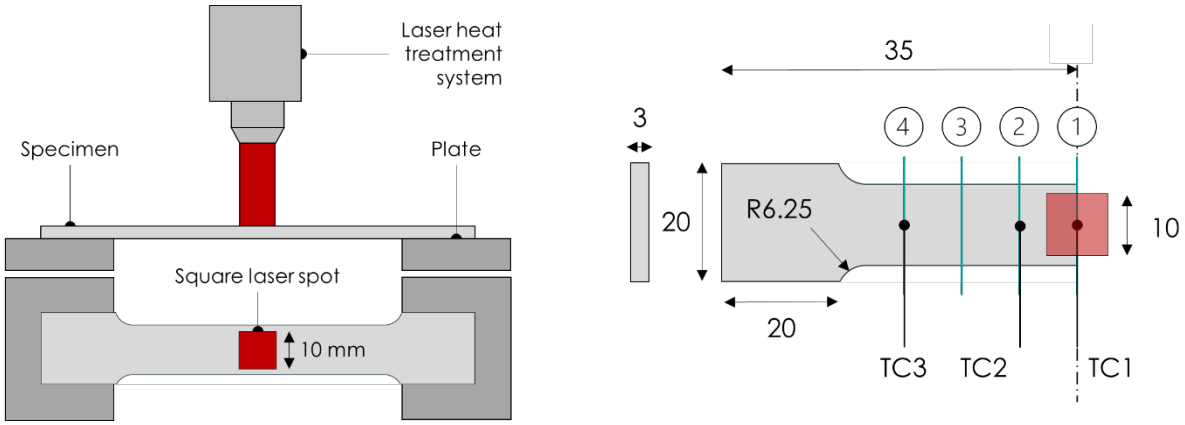

(a) (b)

Fig. 1. LISSF experimental setup (a) and main dimension (mm) of the sample (b) with schematic of section extraction: central slices at 0 mm (1), ±10 mm (2), ±20 mm (3) and ±30 mm (4) from specimen center.

Each experimental laser treatment was carried out three times to ensure repeatability and reliability of the results. A sacrificial sample was used to monitor the temperature (T) along the longitudinal direction during the LISSF using three K-type thermocouples, as illustrated in Fig. *1*b. This allowed the derivation of a fourth-order polynomial (Equation 1) describing the stationary temperature T (°C), after the initial heating step, as a function of longitudinal position (x) within the specimen, enabling direct correlation of measured porosity values after LISSF to process temperature.

$$T = 0.0004x^4 - 1.1898x^2 + 1020 \quad (1)$$

The provided Table 2 outlines the experimental plan designed to analyze the thermal effects on the specimens. This details 12 specific measurement points (ID) characterized by varying dwell times and temperatures distributed along the longitudinal direction of each sample.

The experimental conditions can be categorized into two distinct regions: (i) the zone directly exposed to laser radiation (IDs 1, 5, and 9) and (ii) the zones not exposed (all remaining IDs).

Table 2. Experimental conditions investigated (T: Temperature; DT: Dwell Time).

ID	1	2	3	4	5	6	7	8	9	10	11	12
T, °C	1020	933	672	238	1020	933	672	238	1020	933	672	238
DT, sec	120	120	120	120	240	240	240	240	360	360	360	360

At the end of each test, every specimen was cut to extract transversal slices starting from the center and extending up to 30 mm outward, with a step of 10 mm. The main dimensions of the samples and a schematic of the section extraction is reported in Fig. 1b.

These sections were then prepared metallographically through grinding and polishing to obtain surfaces suitable for microstructural observation.

Subsequently, the prepared sections were analyzed using optical microscopy supported by quantitative image analysis performed using the ImageJ ® software which allowed accurate measurement of P and d values according to both dwell time and temperature. Microhardness tests allowed to determine the mechanical characteristics of the heat-treated material according to the different process conditions. In this regard, measurements were performed using a fully automated Qness Q10 tester in compliance with the Vickers standard (DIN EN ISO 6507).

For each experimental condition, the average Vickers microhardness was calculated from 6 random indentations within the extracted transverse sections, applying a 0.5 kg load by maintaining the load for 15 seconds.

Material Modeling.

As outlined in the introduction, two distinct analytical models were employed to predict the actual material behavior after LISSF: (i) JMAK model with Arrhenius dependence, for describing porosity evolution and (ii) RD model, for correlating microhardness with porosity.

The JMAK approach was adapted to describe the kinetics of porosity growth during solid-state foaming. This model interprets porosity evolution as a sigmoidal process: an initial slow stage, a rapid intermediate growth and a final plateau before pore opening. The Arrhenius dependence accounts for thermal activation, where higher temperatures accelerate creep and superplastic flow, promoting faster pore expansion [7]. The adopted formulations are reported below (Equation 2 and 3).

$$P(t,T) = P_{max}[1 - exp\,(-(k(T)t)^m] \quad (2)$$

$$k(T) = k_0 exp\,(-Q/(RT)) \quad (3)$$

where P is the porosity fraction, P_{max} is representative of the maximum porosity, m is Avrami exponent, k_0 is kinetic factor, Q is activation energy and R is the gas constant (8.314 [J/(mol·K)]). Temperature values are consistently expressed in Kelvin. In more detail, P_{max} represents the structural saturation limit dictated by the alloy's microstructural stability. This parameter is critical for predicting the onset of pore coalescence and potential collapse under prolonged exposure [13]. In agreement with previous findings on high-strength porous Ti–6Al–4V foams synthesized by solid-state powder processing [14], a porosity fraction of approximately 0.50 was considered a suitable compromise between structural integrity and functional performance; therefore, this value was adopted as Pmax in the present study.

Once P is predicted, pore size can be estimated through simple scaling relationships, supporting a comprehensive understanding of foaming behavior.

Finally, assuming that the three-dimensional development of porosity can reasonably be approximated as spherical, the prediction of d (expressed in micrometers) can be directly related to P through a first-order relationship (Equation 4), which is established based on the correlation between the experimental results obtained for the corresponding d and P values:

$$d = 91.964 \cdot P + 7.6611 \quad (4)$$

The RD model explains the exponential decrease in microhardness as porosity increases. According to this approach, the hardness of a porous material (HV) is related (Equation 5) to the hardness of the fully dense material (H_0) through an exponential function, where the sensitivity coefficient (b) quantifies how strongly hardness responds to porosity. For the material investigated in this work, the microhardness of the HIPed condition is equal to 302.5±1.8 μHV0.5; however, to better assess the predictive capability of the model, this value was not directly imposed as a constraint for determining b.

$$H(P) = H_0 e^{b\cdot(P)} \quad (5)$$

In addition to porosity fraction, the model can be adapted to use pore size as a variable (Equation 6), maintaining the same exponential trend. The modified formulation is proposed to account for the average pore diameter, expressed as:

$$H(P) = H_0 e^{b'\cdot(d/100)} \quad (6)$$

where b' is the modified sensitivity coefficient. This approach assumes that pore size can serve as a proxy for porosity, maintaining the exponential decay trend observed in the original RD model. Such a variant is particularly useful when porosity fraction is difficult to measure directly, while pore size distribution is readily available from microstructural analysis.

All constants for both the JMAK and RD models were obtained through direct regression against the full experimental dataset using the Root Mean Square Error (RMSE) minimization, expressed as summarized in the Equation (7).

$$RMSE = \sqrt{\frac{1}{n}\sum_{i=1}^{n}(y_{exp} - y_{mod})^2} \quad (7)$$

where n represents the number of data points, y_{exp} and y_{mod} respectively are the experimental and the predicted (model) values.

Results and Discussion

The results analyze the evolution of P, d and microhardness (μHV0.5) as a function of temperature and dwell time.

Porosity Evolution and Pore Size

The morphological characteristics of the LISSF specimens; specifically, P and d, are presented in Fig. 3.

The material exhibits markedly different responses under the two thermal exposure conditions. At 1020 °C, which corresponds to the center of the specimen directly exposed to the laser radiation, the material exhibits a significant foaming effect. P (Fig. 3a) at this temperature ranges from 0.263 (dwell time equal to 120 s) to 0.30 (360 s).

Conversely, the regions not directly exposed to laser irradiation (933 °C, 672 °C, and 238 °C) exhibit a marked reduction in porosity, stabilizing below 0.05 regardless of the dwell time, as also supported by the micrographs shown in Fig. 2.

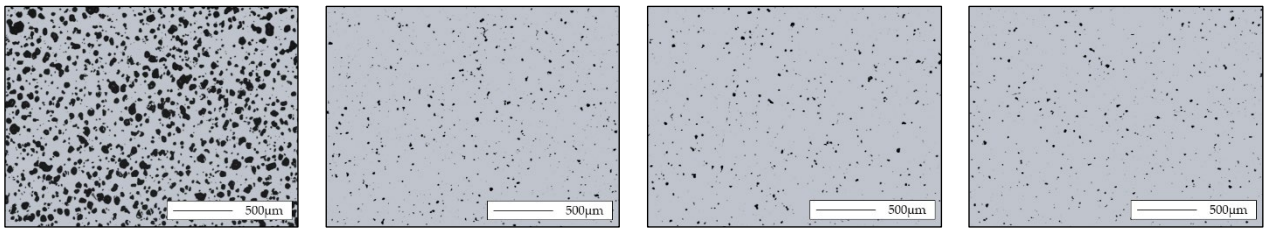

1020°C *933°C* *672°C* *238°C*

Fig. 2. Micrographs referring to a LISSF in which a temperature of 1020 °C was set at the laser position for a total dwell time of 120 s.

This observation suggests that the activation energy – or the thermal threshold required for significant pore expansion – is primarily achieved under direct laser exposure. Indeed, this assumption is supported by comparing the porosity obtained at the same temperature when using a conventional furnace heating process, already documented in a previous work [12], with that obtained using laser-based heating. When the two conditions reported below (Table 3) are compared, despite the SSF temperature being the same (1020 °C), a markedly greater capability for pores to grow in size can be observed in the case of LISSF, despite the much longer exposure (3600 s) at high temperature experienced by the furnace-heated sample.

Table 3. Comparison between SSF in furnace and LISSF at 1020 °C.

	Temperature, °C	Time, s	P	d, μm
Furnace	1020	3600	0.17	11.00
LISSF	1020	120	0.26	33.17

Regarding d, shown in Fig. 3b, a similar trend was recorded. The area subject directly to the laser irradiation result in significantly larger pores, with diameters ranging between 33.17 (dwell time equal to 120 s) and 34.89 µm (360 s) at 1020 °C.

A slight time-dependence is observed in the direct interaction zone. As the dwell time increases from 120 s to 360 s, the average pore diameter shows a moderate increase. This is likely attributable to the coalescence of pores (Ostwald ripening) [15].

At lower temperatures (238°C - 933°C), the pore diameter remains relatively constant and small (12-13 µm), indicating that the only conduction heating alone is insufficient to drive further pore growth or coalescence.

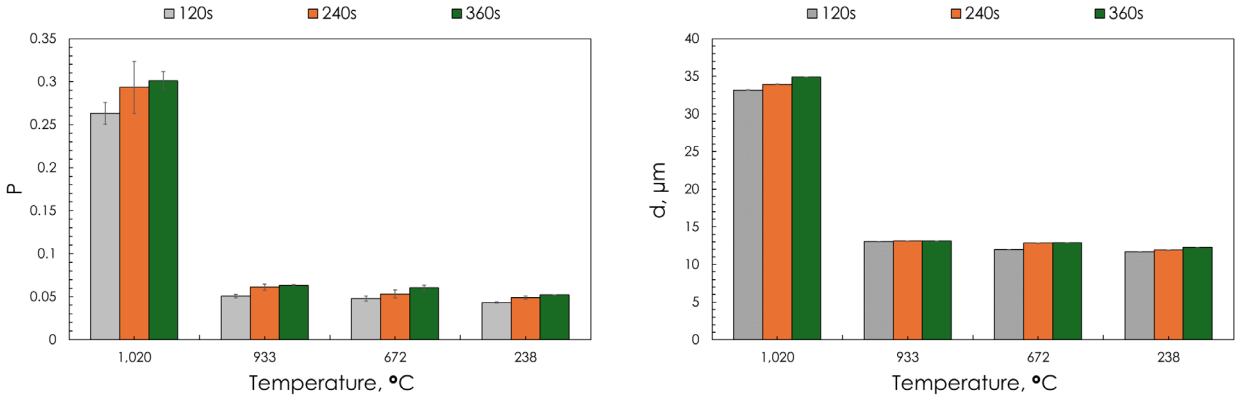

(a) (b)

Fig. 3. Experimental results in terms of (a) P and (b) d according to the different temperature and dwell time investigated.

Microhardness Analysis.

The mechanical response of the investigated Ti alloy was evaluated through Vickers microhardness testing, as illustrated in Fig. 4. The microhardness exhibits an inverse relationship with the processing temperature and the resulting porosity.

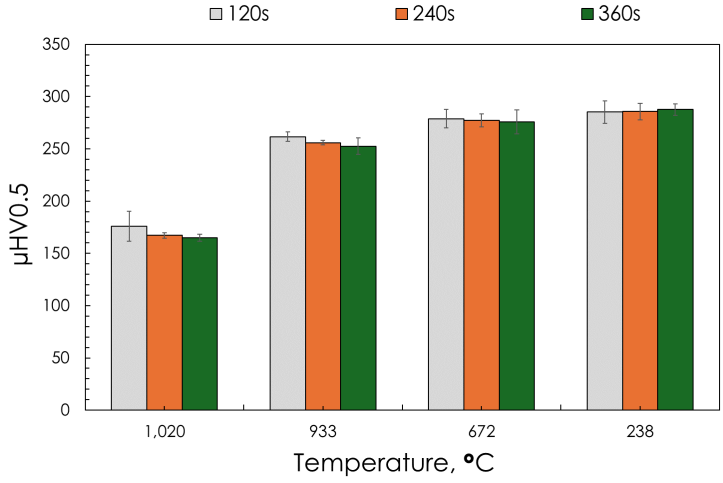

Fig. 4. Experimental results in terms of Vickers microhardnesses according to the different temperature and dwell time investigated.

The lowest hardness values, ranging between 165 (dwell time equal to 360 s) and 175 HV (360 s), are recorded at 1020°C. This softening can be attributed to the high-volume fraction of porosity which reduces the effective load-bearing area. As the distance from the laser spot increases (temperature decreases), the microhardness recovers significantly. At 933 °C, values range from 252.6 to 261.6 HV and they reach a maximum of nearly 290 HV at 238 °C. When compared to the effect of

temperature, the dwell time appears to have a minor influence on microhardness within the examined range, particularly in the peripherical area of each specimen.

In general, the data confirms that the LISSF is highly localized. Effective foaming, characterized by high porosity (P greater than 0.25) and large pores (d greater than 30 μm), is restricted to the direct laser irradiation zone (1020°C). The surrounding material retains a denser structure and higher mechanical hardness, resembling the AR properties of the alloy.

Material Modeling Results.

The analysis compares the experimental data (Exp) with the numerical predictions (Model) for P, d and the resulting microhardness (μHV0.5).

Porosity Modeling.

As outlined earlier, P was modeled using the JMAK (Johnson-Mehl-Avrami-Kolmogorov) approach. The accuracy of the model was evaluated separately for two distinct regions: (i) the zone directly exposed to laser radiation (IDs 1, 5, and 9) and (ii) the zones not exposed (all remaining IDs). The identification of separate model parameters for the exposed and unexposed zones is required due to the fundamentally different thermal profiles and kinetic mechanisms governing pore evolution in the two regions. Direct laser irradiation produces extremely high heating rates and steep thermal gradients, reaching temperatures near or above the β-transus and activating diffusion- and creep-based expansion mechanisms that are not observed under conduction-based heating [7,16,17]. Consequently, porosity evolution follows distinct kinetic paths and a single parameter set would not be able to simultaneously reproduce the behavior of both regimes while maintaining physical consistency and predictive accuracy.

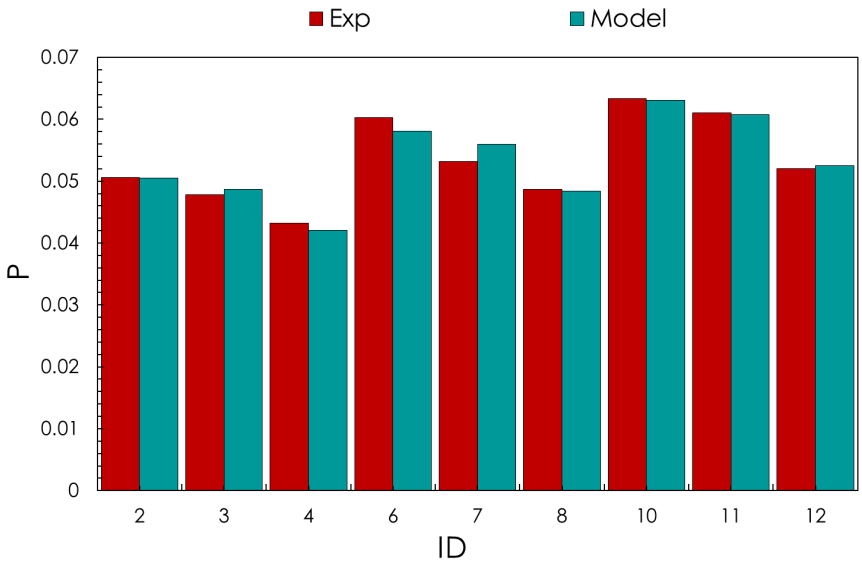

Fig. 5. JMAK model (Equations 2 and 3) prediction for P with reference to the zones not exposed to the laser radiation.

The model predictions for the zones not exposed show a strong correlation with the experimental findings. The bar chart comparison indicates that the modeled values (Model) closely track the experimental porosity (Exp) across the identified samples. The linear regression analysis confirms this agreement, yielding a RMSE of 0.959.

Table 4 summarizes the values of the constants determined considering Equations (2 and 3).

Table 4. Constant of JMAK model for P with reference to the zones not exposed to the laser radiation.

P_{max}	K_0, s^{-1}	m	Q, J/mol	RMSE
0.5	0.04434	0.213	6686.9	0.959

For the samples directly exposed to the laser spot (1020°C), the model demonstrates excellent predictive capability. The comparison between experimental and modeled P reveals negligible deviation. The linear regression analysis for this regime exhibits a perfect fit with an RMSE of 1, suggesting that the JMAK model captures the porosity evolution under direct laser exposure with high precision. Although the laser-exposed region provides only three experimental porosity values, these points span a broad temporal range (120, 240 and 360 s) and appear to be sufficient to identify the two unknown parameters of the JMAK law at constant temperature. Indeed, at fixed value of temperature the model reduces to a two-parameter problem (k and m).

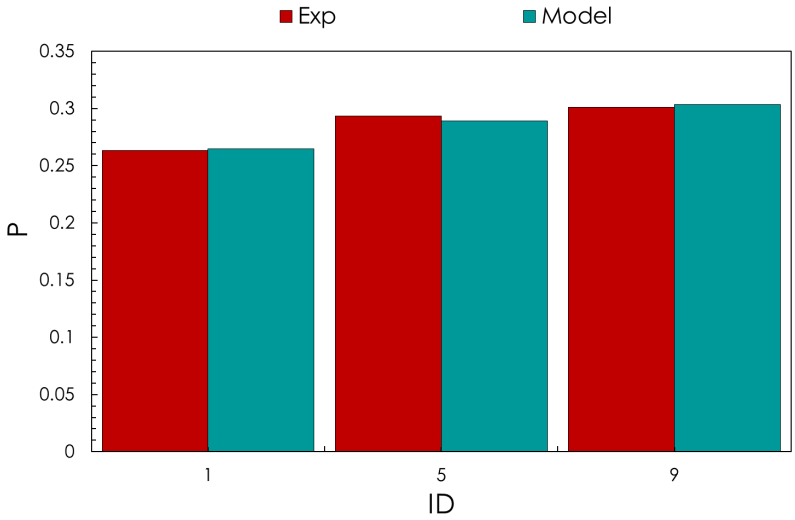

Fig. 6. JMAK model (Equations 2 and 3) prediction for P with reference to the zones directly exposed to the laser radiation.

Table 5 summarizes the values of the constants determined according to the laser regime.

Table 5. Constant of JMAK model for P with reference to the zones directly exposed to the laser radiation.

P_{max}	K_0, s^{-1}	m	Q, J/mol	RMSE
0.5	2.383	0.195	114937.2	1.000

Laser heating produced localized high temperatures near the β-transus (about 980 °C), resulting in greater deformability and significantly faster kinetics compared to conduction heating [16]. This effect stems from rapid thermal cycling and high peak temperatures that activate more dynamic nucleation and growth processes in the β-phase. As a result, laser-treated samples exhibit significantly higher porosity under identical process durations [17]. Consequently, laser-treated regions reached higher porosity levels within the same time frame. The model is effective because it captures the observed trend with few parameters that have clear physical meaning, such as the Avrami exponent (growth mechanism), activation energy (thermal sensitivity) and maximum porosity (structural limit).

The modeling of d also displays a high degree of accuracy when compared to the experimental measurements (Exp). The bar chart comparison shows that the model correctly predicts the significant variation in pore sizes, particularly distinguishing between smaller pores (about 12 μm) and larger pores (33-35 μm) found in specific samples (e.g. IDs 1, 5, 9) directly exposed to the spot laser action.

The linear regression analysis for p yields an RMSE of 0.997, confirming that the model effectively replicates the experimental trends regarding the dimensional growth of the porosity.

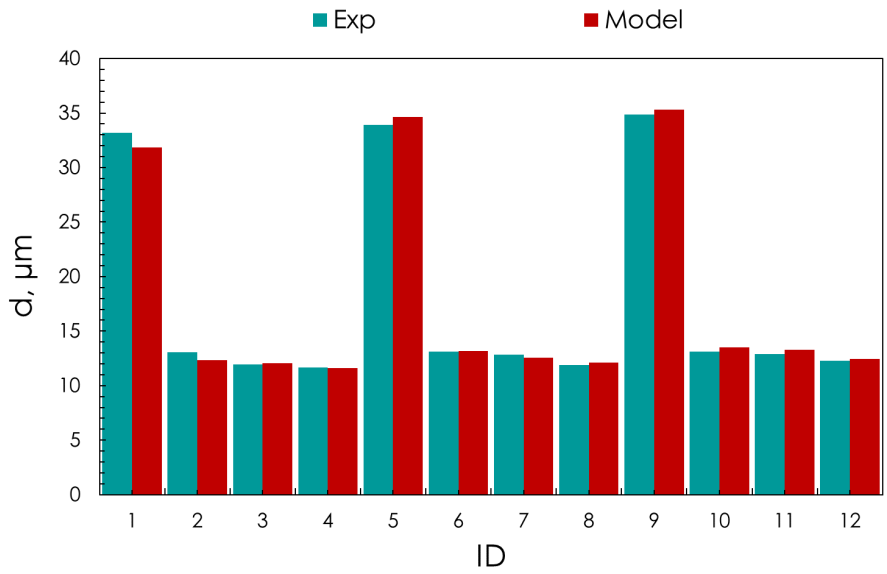

Fig. 7. Empirical model (Equation 4) prediction model for d.

Microhardness Modeling.

The comparison between experimental Vickers microhardness (Exp) and the model predictions (Model) shows consistent agreement across all tested conditions, with values generally ranging between 170 and 280 HV. As porosity grows, the effective load bearing area is reduced and stress effects become more prominent, leading to a loss in hardness even for small increments of porosity. This behavior aligns with the principles of cellular solids described by Gibson and Ashby [13].

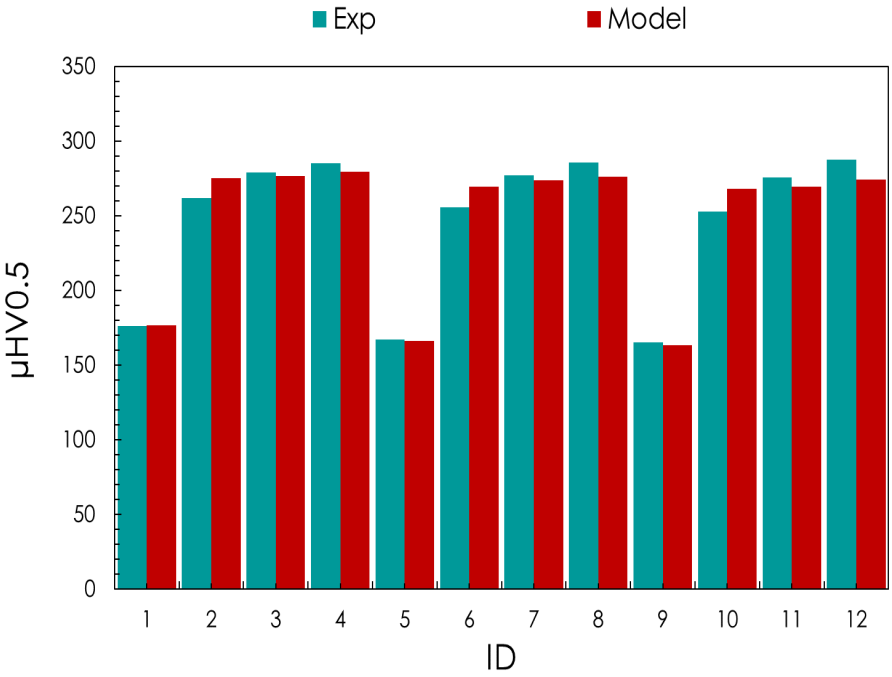

Fig. 8. RD model (Equation 5) prediction for P.

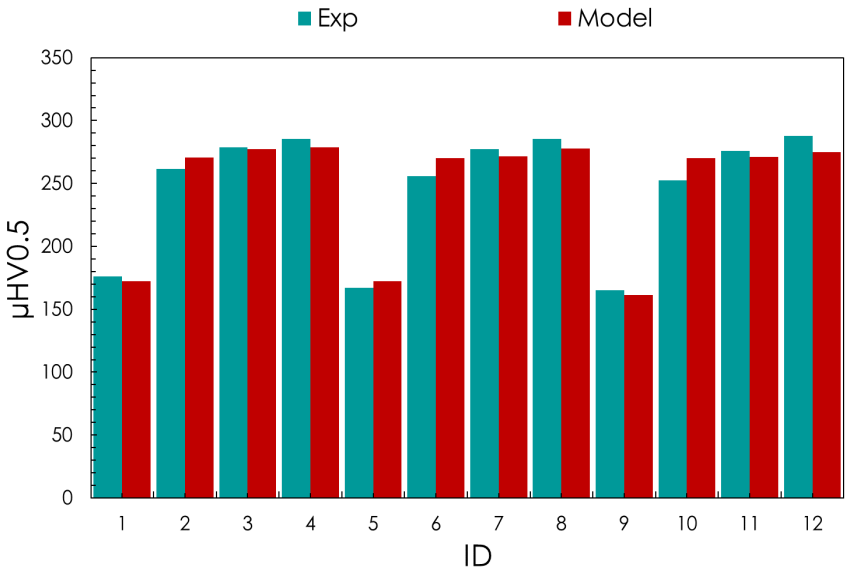

Fig. 9. Modified RD model (Equation 6) prediction for d.

The regression analysis for the microhardness data yields an RMSE of 0.962 as regard P (Fig. 8) and similarly equal to 0.9631 in the subsequent analysis for d (Fig. 9), indicating that the material modeling approach successfully predicts the mechanical property changes induced by the thermal cycles.

Table 6 summarizes the values of the constants determined with reference to both P and d considering Equations (5 and 6). Although the calibrated values of b and b′ are very close to each other, the value of H_0 obtained for the model associated with P is almost identical to the experimental one (302.5 vs 305.6), demonstrating a strong predictive capability.

Table 6. Constant of RD model for both P and d.

Variable	H_0, µHV0.5	b	b', μ^{-1}
P	305.6	2.1	-
d	362.1	-	2.2

Conclusion

In the present work, the feasibility of a LISSF process for HIPed Ti6Al4V-ELI alloy was successfully demonstrated. The study investigated the effects of laser processing parameters on the reactivation and growth of argon-filled pores, leading to the following assessments:

- The LISSF technique allows for the generation of porous structures with tunable characteristics. A direct correlation was established between the input energy (governed by controlled laser power to reach a constant temperature) and the resulting porosity. Higher temperatures and prolonged exposure times promoted significant pore expansion, transforming the material from a nearly fully dense state to a porous structure suitable for biomedical applications.
- Two distinct heating regimes were identified according to two different regions of the LISSFed specimens: (i) the region directly exposed to laser irradiation and (ii) the adjacent region outside this exposure. The first region exhibited the highest porosity fractions (up to 0.30) and larger pore diameters, whereas the other one showed finer and more uniformly distributed porosity, underscoring the potential for designing functionally graded materials.

- A kinetic model based on the JMAK equation was successfully applied to predict both the porosity fraction (P) and the average pore diameter (d). The model showed excellent agreement with experimental data (RMSE greater than 0.95) for both variables and laser heating regimes. Furthermore, a linear relationship was validated to predict the microhardness evolution as a function of the thermal history.
- Complementarily, R-D model provided a robust description (RMSE greater than 0.96) of the mechanical response, confirming the exponential decay of microhardness with increasing porosity and pore size.

In conclusion, LISSF of HIPed titanium offers a promising, flexible route to manufacture components with locally tailored porosity, bridging the gap between solid, structural parts and porous, osseointegrative surfaces. Future developments will focus on calibrating models capable of predicting additional mechanical properties – such as elastic modulus, yield strength, ultimate tensile strength (UTS) and elongation at fracture – based on the porosity observed after LISSF, as well as on optimizing scanning strategies for the fabrication of complex 3D-graded lattice structures.

References

[1] Miko T, Petho D, Gergely G, et al. A Novel Process to Produce Ti Parts from Powder Metallurgy with Advanced Properties for Aeronautical Applications. Aerospace. 2023;10(4).

[2] Yang XL, Du XF, Xu ZL, et al. Progress in processing of porous titanium: a review. Rare Metals. Springer; 2024. p. 1932–1955.

[3] Yadav MK, Yarlapati A, Aditya YN, et al. Processing and Development of Porous Titanium for Biomedical Applications: A Comprehensive Review. Journal of Manufacturing and Materials Processing [Internet]. 2025;9(12):401.

[4] Wu D, Li Y, Zhu W, et al. Fabrication and biocompatibility of a 3D-printed porous Ti-25Ta alloy scaffold. Discover Applied Sciences. 2025;7(7).

[5] Tian JH, Li YH, Wu XJ. Research Progress on Biocompatible Sintered Porous Titanium Alloys for Hard Tissue Implants. Transactions of the Indian Institute of Metals. Springer; 2025.

[6] Guglielmi P, Piccininni A, Cusanno A, et al. Manufacturing of a hybrid component in Ti6Al4V-ELI alloy by combining diffusion bonding and superplastic forming. Materials Research Proceedings. Association of American Publishers; 2023. p. 37–44.

[7] Oppenheimer S, Dunand DC. Solid-state foaming of Ti-6A1-4V by creep or superplastic expansion of argon-filled pores. Acta Mater. 2010;58(13):4387–4397.

[8] Murray NGD, Dunand DC. Effect of initial preform porosity on solid-state foaming of titanium. J Mater Res. 2006;21(5):1175–1188.

[9] Duckworth W. Discussion of Ryshkewitch Paper by Winston Duckworth. Journal of The American Ceramic Society-Ryshkewitch. Vol. 36, No. 2.

[10] Ryshkewitch E. Compression Strength of Porous Sintered Alumina and Zirconia. 1953.

[11] Fanfoni M, Tomellini M. The Johnson-Mehl- Avrami-Kohnogorov model: A brief review. Il Nuovo Cimento D [Internet]. 1998;20(7):1171–1182.

[12] Guglielmi P, Palumbo G. Production of porous titanium structures by combining hot isostatic pressing and solid-state foaming. CIRP J Manuf Sci Technol. 2024;52:58–72.

[13] Gibson LJ, Ashby MF. Cellular Solids: Structure and Properties [Internet]. 2nd ed. Cambridge Solid State Science Series. Cambridge: Cambridge University Press; 1997. Available from: https://www.cambridge.org/core/product/BC25789552BAA8E3CAD5E1D105612AB5.

[14] Lee MH, Kim KB, Han JH, et al. High strength porous Ti–6Al–4V foams synthesized by solid state powder processing. J Phys D Appl Phys [Internet]. 2008;41(10):105404.

[15] Yu W, Zhou X, Kanj MY. Microfluidic Investigation of Foam Coarsening Dynamics in Porous Media at High-Pressure and High-Temperature Conditions. Langmuir. 2022;38(9):2895–2905.

[16] de Freitas FE, da Silva RAL, Takahashi RJ, et al. Influence of Laser Remelting on Creep Resistance in Ti-6Al-4V Alloy with Thermal Barrier Coating. Coatings. 2025;15(2).

[17] Cerri E, Ghio E. On Strain-Hardening Behavior and Ductility of Laser Powder Bed-Fused Ti6Al4V Alloy Heat-Treated above and below the β-Transus. Materials. 2024;17(14).